

## Computational Anatomical Analysis of the Basal Forebrain Corticopetal System

---

Laszlo Zaborszky, Attila Csordas, Derek L. Buhl,  
Alvaro Duque, Jozsef Somogyi, and Zoltan Nadasdy

### ABSTRACT

The basal forebrain (BF) is comprised of a neurochemically heterogeneous population of neurons, including cholinergic, GABA-ergic, peptidergic, and possibly glutamatergic neurons, that project to the cerebral cortex, thalamus, amygdala, posterior hypothalamus and brain stem. This multitude of ascending and descending pathways participate in a similarly bewildering number of functions, including cognition, motivation, emotion, and autonomic regulation. Traditional anatomical methods failed to grasp the basic organizational principles of this brain area and likened it at best to the organization of the brain stem reticular formation. Our studies, using various computational methods for analyzing the spatial distribution and numerical relations of different chemically and hodologically characterized neuronal populations, as well as fully reconstructed electrophysiologically identified single neurons, began to unravel the organizational principles of the BF. According to our model, the different cell types form large-scale cell sheets that are aligned to each other in a specific manner. Within each cell system, the neurons display characteristic discontinuous distributions, including high density clusters. As a result of nonhomogeneity within individual cell populations and partial overlapping between different cell types, the space containing the bulk of cholinergic neurons comprises a mosaic of various size cell clusters. The composition, dendritic orientation, and input–output relationships of these high density cell clusters show regional differences. It is proposed that these clusters represent specific sites (modules) where information processed in separate streams can be integrated. Via this BF mechanism a topographically organized prefrontal input could allocate attentional resources to cortical associational areas in a selective self-regulatory fashion.

### 9.1. INTRODUCTION

The term basal forebrain (BF) refers to a heterogeneous collection of structures located close to the medial and ventral surfaces of the cerebral hemispheres. This highly complex brain region has been implicated in attention, motivation, and memory as well

From: *Computational Neuroanatomy: Principles and Methods*  
Edited by: G. A. Ascoli © Humana Press Inc., Totowa, NJ



as in a number of neuropsychiatric disorders such as Alzheimer's disease, Parkinson's disease, and schizophrenia (1-3). Part of the difficulty in understanding the functions of the BF, as well as the aberrant information processing characteristic of these disease states, lies in the anatomical complexity of the region. BF areas, including the medial septum, ventral pallidum, diagonal band nuclei, substantia innominata, and peripallidal regions contain cell types different in transmitter content, morphology, and projection pattern (4,5). Among these different neuronal populations, the cholinergic corticopetal neurons have received particular attention in numerous functional and pathological studies.

Recent interest in BF research was prompted by discoveries showing that a specific population of neurons in this region, namely those that use acetylcholine as their transmitter and project to the cerebral cortex, are seriously compromised in Alzheimer's disease (6-9). However, cholinergic projection neurons represent only a fraction of the total cell population in these forebrain areas, which also contain GABA-ergic, peptidergic, and possibly glutamatergic neurons (10,11). According to our unpublished estimations in one hemisphere of the rat brain, in the cholinergic BF areas, 20,000 cholinergic corticopetal cells are intermingled with other neurons, including about 35,000 calbindin, 26,000 calretinin, and 24,000 parvalbumin-containing neurons. These calcium-binding proteins are used to characterize different nonoverlapping populations of non-cholinergic BF neurons.

A quasi 3D representation of the cholinergic cell bodies (Fig. 1A) or the dendritic arborizations of their neurons (Fig. 1B) does not appear to show any recognizable architectural features, confirming a classical view in the literature that arousal is supported by a diffuse reticular activating system, including core brain stem structures, the BF, and the so-called nonspecific thalamic nuclei (12,13). On the other hand, careful monitoring of the behavioral effects of lesions in the BF using an immunotoxin selective for cholinergic neurons, suggests that compartments of the BF, together with their specific cortical target areas, may participate in different cognitive operations (14).

If the BF participates in different operations, we would expect that this may be reflected both in the local, as well as in the large-scale structural organization of its constituent neuronal populations. For example, one would expect that the BF would be constituted of repetitive building blocks (modules) as found in many other areas of the central nervous system (CNS), including the cortex, striatum, hypothalamus, brain stem, or the spinal cord (15-18). The modular structure in various brain regions is the prerequisite structural basis for parallel, distinct operations (19). Other structural features, like anisotropic dendritic orientation or segregation of various afferents and efferents, can also be taken as evidence for selective information processing (20-26). In the past several years, we systematically investigated the 3D spatial organization of the various BF neural populations, including their dendritic organization and input-output relationship with the aim of uncovering the organizational principles of the BF, in particular within areas that are most heavily populated by cholinergic corticopetal neurons. This review is an attempt to summarize how anatomical features may constrain information processing in this brain area. The chapter is divided into several sections, each with subheadings indicating the special methods used. Following the main body of the text, the reader can find an Appendix with a detailed explanation of the data acquisition and methods analysis presented.



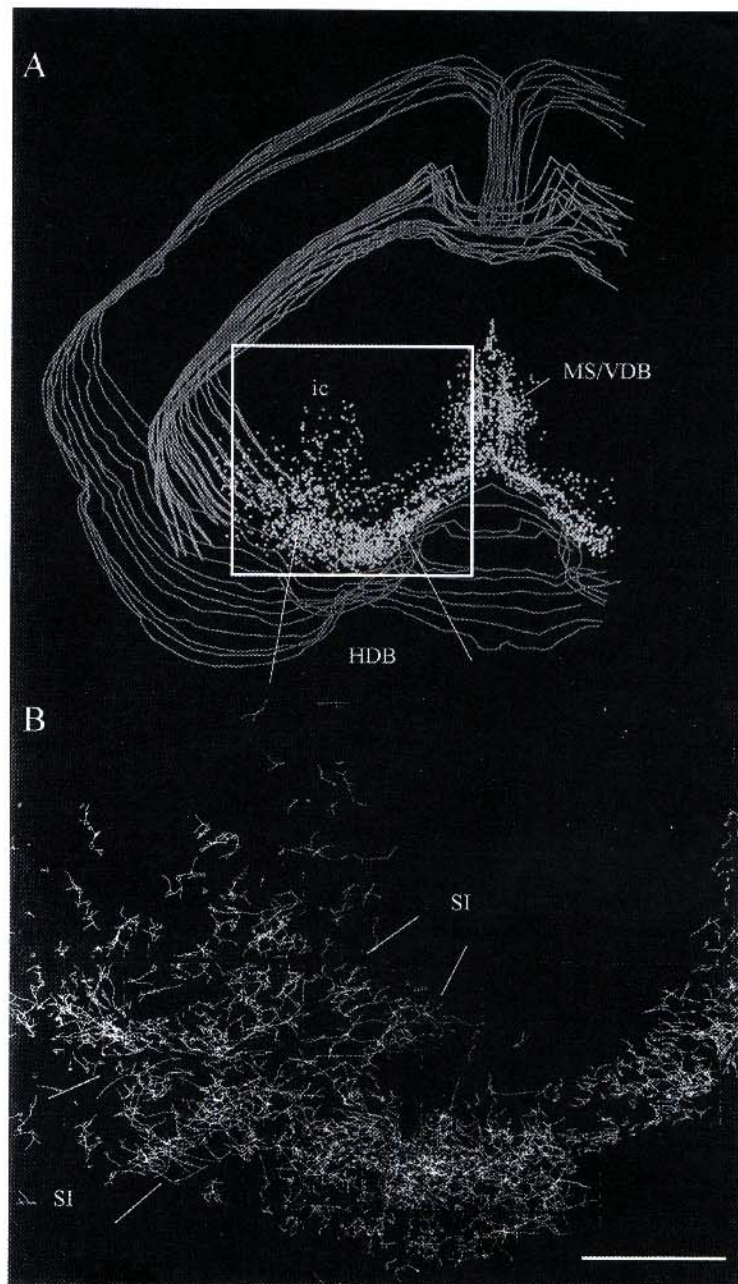


**Fig. 1.** (A) 3D wireframe diagram showing the distribution of cholinergic neurons in the BF. Cholinergic cells (dots) were mapped from 12 sections, approx 300 μm apart. The contours of the corpus callosum and the section outlines are marked. (B) Composite map illustrating the dendritic architecture of the BF cholinergic system. The location of panel B corresponds to the enclosed box in panel A. Dendrites of approximately 1300 cholinergic neurons were traced from 7 coronal sections. Diagonal white lines delineate the approximate location of the corresponding major forebrain areas. HDB, horizontal limb of the diagonal band; ic, internal capsule; MS/VDB, medial septum/vertical limb of the diagonal band; SI, substantia innominata. Scale bar, 1 mm (applies only to panel B). A color version of this figure is enclosed in the CD-ROM.



## 9.2. ASSOCIATION AND SEGREGATION OF DIFFERENT HODOLOGICALLY IDENTIFIED NEURAL POPULATIONS

### 9.2.1. *Overlap Analysis*

Although there is considerable species variation in the precise locations of cholinergic projection neurons in the BF, the efferent projections of these cells follow basic organizational principles in all vertebrate species studied. Thus in rodents, neurons within the medial septum and nucleus of the vertical limb of the diagonal band provide the major cholinergic innervation of the hippocampus; cholinergic cells within the horizontal limb of the diagonal band project to the olfactory bulb, piriform and entorhinal cortices; cholinergic neurons located in the ventral pallidum, sublenticular substantia innominata, globus pallidus, internal capsule, and nucleus ansa lenticularis, collectively termed as nucleus basalis, project to the basolateral amygdala and innervate the entire neocortex according to a rough mediolateral and anteroposterior topography (27–35). Similarly, in primates, including humans, corticopetal cholinergic cells are subdivided according to the topography of their projections (36).

It is unclear, however, what the functional equivalent of this topography is, especially in light of a study in rat, showing that neighborhood relationships in the BF projection neurons do not correspond to near neighbors in the representational areas of sensorimotor cortices, thus arguing against a simple functional organization (37). Knowing the importance of the cholinergic BF system in modulating cortical activity (38), we asked whether the organization of the basalocortical system can, in any sense, be related to the distributed and hierarchical organization of corticocortical connections, as proposed by Felleman and Van Essen (39). Figures 2 and 3 display cases of overlapping and segregated projection neurons from a study aiming at a comprehensive reevaluation of the basalocortical projection (Csordas and Zaborszky, in preparation). Figure 2A is from a case in which two different retrograde tracers were injected into two cortical areas that were in the same mediolateral topographical register but they differed in their rostrocaudal location. This 3D image suggests that the two neuron populations (marked by different symbols<sup>1</sup>), projecting to two cortical areas, are, at least in the rostral part of the BF, intermingled. Using an overlap analysis program described recently (21,25,40), Figure 2C shows that a substantial population of the two types of projection neurons are, indeed, located in overlapping voxels<sup>2</sup> (the method is briefly described in Appendix 9.9.4.). Figure 2B shows another case in which the two retrograde tracer injections were in different mediolaterally located cortical areas. As can be seen from this 3D rendering, there is little overlap in the location of the neurons projecting to these two cortical target areas. Figure 2D, using the overlap analysis program, supports the subjective impression that no overlap exist between these two distinct cell populations.

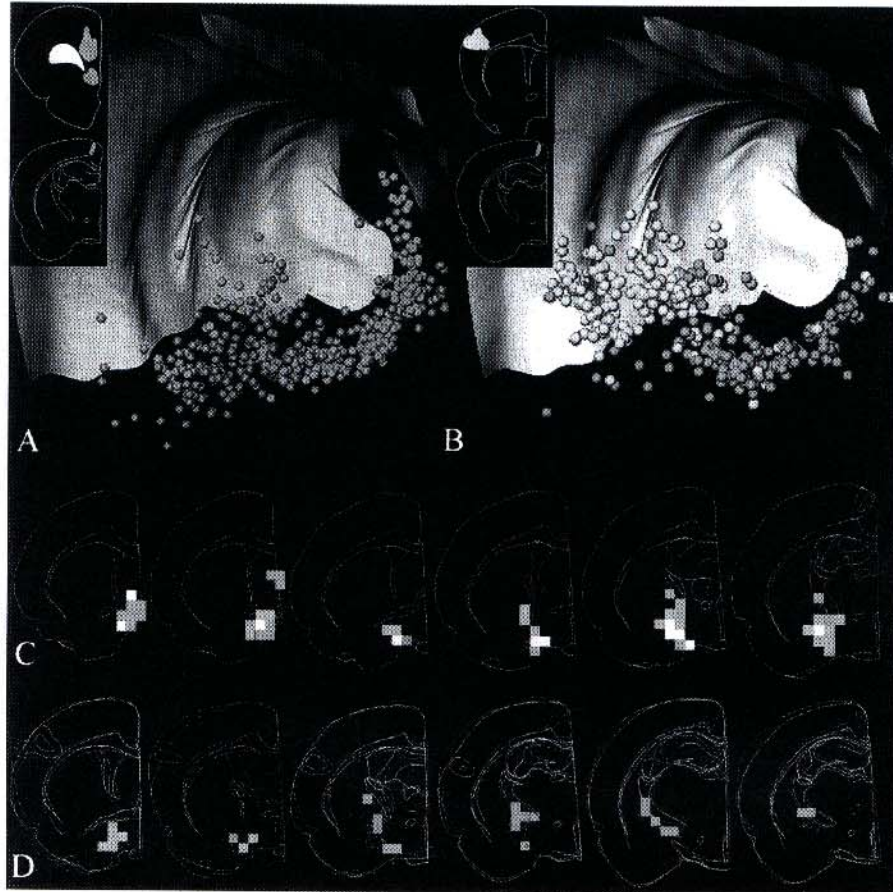
### 9.2.2. *Isodensity Surface Rendering*

Figure 3A shows a 3D rendering of the distribution of four BF cell populations that project to four arbitrarily defined mediolateral sectors of the neocortex reconstructed

<sup>1</sup>A color version of this and other figures are available in the companion CD-ROM file.

<sup>2</sup>Voxel is a 3D pixel that is the spatial unit of our analysis. See also Appendix 9.9.4. A mathematical description of the definition of voxels can be found in (41).





**Fig. 2.** (A) Distribution of non-cholinergic neurons projecting to the medial prefrontal cortex (light) and the border region between M1 and M2 region (dark). Note the substantial overlap of light and dark cells in the rostral (right hand side of the model) BF. Fluoro-Gold was injected into two sites in the prefrontal cortex and Fast Blue into the border of the M1/M2 regions (upper left insets). (B) Distribution of cholinergic neurons projecting to the somatosensory (light) and the M1/M2 association region (dark). Note the apparent minimal overlap between the light and dark symbols in the basal forebrain. (C) Overlap analysis from selected sections of case shown in panel A. (D) Overlap analysis from the case depicted in B. For panels C and D, each section was subdivided into  $500 \times 500 \times 50 \mu\text{m}$  voxels, and the number of cells from each of the two populations (populations "1" and populations "2") was counted in each voxel. Voxels containing at least 3 cells of either population are marked with light gray and dark gray, respectively; those containing at least 3 of both marker types are marked in white. Note the substantial overlap in panel C, as indicated by the white voxels. In panel D, no white voxels are detected indicating no overlap in this case. Note that the gray scalings (colors in the companion CD-ROM file) of the voxels here represents population "1" and/or population "2" and does not correspond to the coding in panels A and B. The corpus callosum is rendered by double gray/white surfaces around the cingulum bundle in the 3D models. A color version of this figure is enclosed in the CD-ROM.

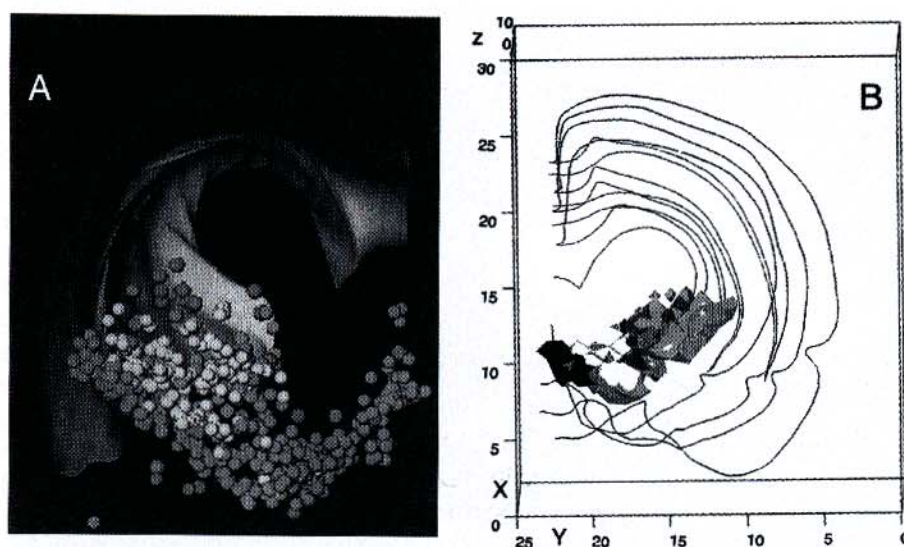


**Fig. 3.** (A) Composite map showing the 3D distribution of cholinergic cells projecting to four arbitrarily defined mediolateral sectors of the neocortex. In the color version of this figure (accompanying CD-ROM), cells projecting to different regions are color-coded (medial, red; intermediary sector, blue and yellow; and lateral parts of the neocortex, green). Note the relatively ordered rostromedial to caudolateral distribution of cells that project to mediolaterally located cortical areas. Dark (red) symbols in the lower right side of the model are rostral. Medial is right, lateral is left. (B) Isodensity surface rendering to show the major organizational features in the BF. Unit space:  $400 \times 400 \times 50 \mu\text{m}$ , density threshold  $\geq 2$  cell/voxel. For appreciation of the different cell groups see the color version of this figure where dark blue surface covers unit spaces that contain cholinergic cells projecting to the posteromedial (M1/M2) cortex; yellow, medial prefrontal cortex; red, barrel cortex; green, posterior insular-perirhinal; light blue, agranular insular-lateral orbital; magenta, lateral frontal (motor) cortex. The isorelational rendering of panel B is placed into the wireframe of the section outlines and the corpus callosum to show their real position in the original brain. Note that the view in panel B is a mirror image of panel A. Here and at the rest of the 3D representations, the numbers along the z axis are the layers (sections), and the x and y values correspond to the voxel indices. A color version of this figure is enclosed in the CD-ROM.

from eight individual experiments. Since the overlap analysis is limited to the simultaneous comparison of only two cell populations and only in two dimensions, in order to appreciate the overall projection pattern in the 3D space, we developed an algorithm that renders a surface around voxels of similar cell densities (Appendix 9.9.4. and [41]). Since cells are replaced by densities, and densities are rendered around by surfaces, the simultaneous 3D visualization of multiple cell populations is feasible. Figure 3B is a 3D composite of the isodensity maps of six different cell populations, suggesting that the bulk of each cell population projecting to the six cortical targets is separated in the BF. Unfortunately, when isosurfaces of different cell types are combined, the larger surface area may have included isosurfaces of other cell types. Therefore, separate renderings of the individual cell populations and pairwise overlap analysis have to be considered (41).



A detailed overlap analysis of 9 cases, each with paired injections, and some 30 computer-generated combinations of these cases (Csordas and Zaborszky, in preparation) suggest that corresponding mediolaterally located frontal and posterior cortical areas receive their input from a partially overlapping area in the BF. On the other hand, topographically noncorresponding frontal and parieto-insular areas receive their projections from nonoverlapping areas of the BF. Since the location of overlapping voxels in the BF is highly specific for the injection sites that represent cortical associational columns, these data suggest that the BF cholinergic input is transferred via specific corticocortical nodal points toward hierarchically related frontal cortical areas.

### 9.3. INHOMOGENEOUS DISTRIBUTION OF CHEMICALLY IDENTIFIED CELL POPULATIONS

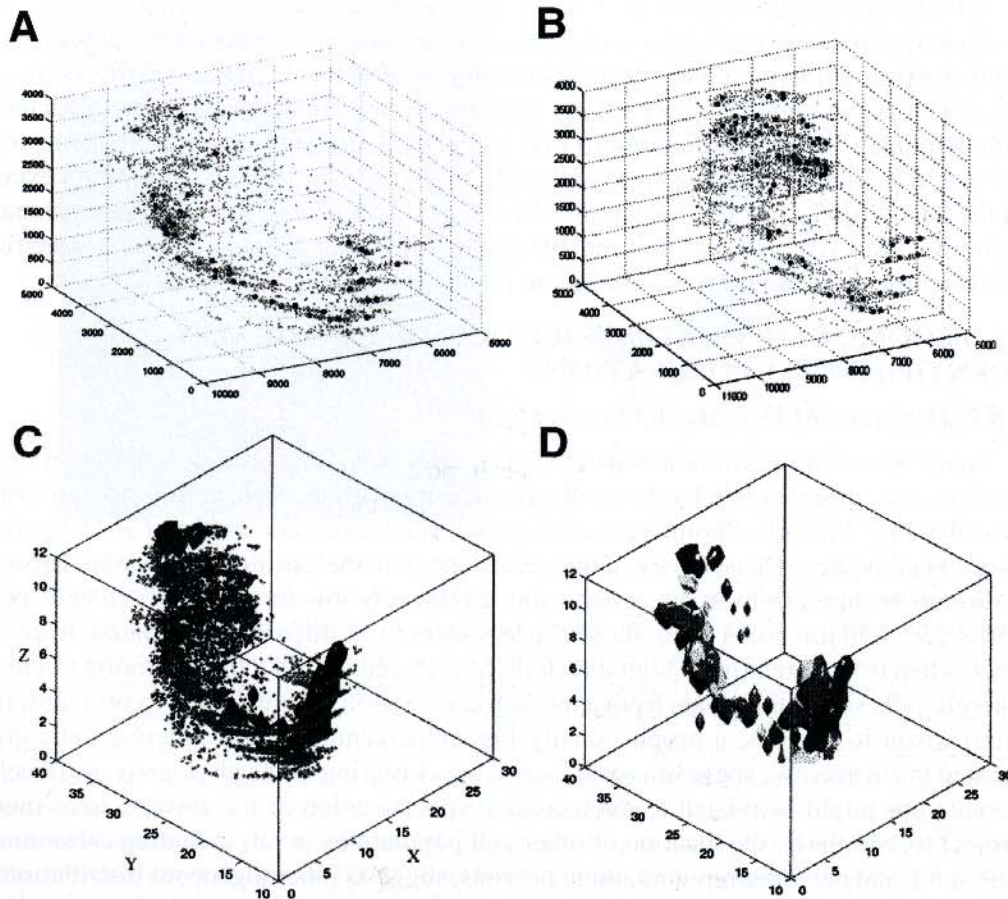
#### 9.3.1. Differential Density 3D Scatter Plot

Figure 4A, using a differential density 3D scatter plot (for a brief description of this method, see Appendix 9.9.4.) shows that the density of cholinergic cells is not uniform (see also Fig. 2 in [4]). Cholinergic cells often form clusters consisting of 3–15 tightly packed cell bodies. The saliency of these clusters, nonetheless, depends on the density threshold setting. For example, when using a relatively low threshold ( $d \geq 5$  cells per  $250 \times 250 \times 50 \mu\text{m}$  voxel size), these clusters seem to be diffusely distributed. In contrast, when using a relatively high threshold ( $d \geq 15$  cells/voxel), the clustering of cholinergic cells seems to deviate from a random distribution. Interestingly, in primates, in comparison to rodents, a proportionally higher percentage of cholinergic cells are located in clusters (4), suggesting that increasing clustering in the phylogeny of BF cell populations might be related to the increased specialization of the cortical areas they project to. Similarly, the location of other cell populations in rat, including calretinin, calbindin, and parvalbumin-containing neurons, suggests inhomogeneous distributions (Zaborszky, Buhl, Pabalashingham, Somogyi, Bjaalie, and Nadasdy, in preparation). Figure 4B shows a similar type of differential density scatter plot of parvalbumin-containing neurons, where dots represent the cell bodies, and large filled circles represent high density spots.

#### 9.3.2. Isorelational Surface Rendering

Since the simultaneous visualization of more than two populations using differential density scatter plots is difficult, we applied another surface rendering algorithm that uses both density and spatial relational constraints (Appendix 9.9.4. and [41]). Figure 4C shows the isorelational surfaces (dark solid) rendered around regions where the density of both cholinergic and parvalbumin cells met two criteria: (i) density is at least five for each cell type within the voxel ( $250 \times 250 \times 50 \mu\text{m}$ ); and (ii) the ratio of cholinergic to parvalbumin cell counts is at least 0.5. In other words, the voxels covered by the dark surface contain at most twice as many parvalbumin as cholinergic neurons. With the isorelational surface rendering, we introduced double constraints, density and relational, which led to a further simplification of our model. Comparing the locations covered by such isorelational surfaces with the scatter plot distribution of the corresponding two-cell populations clearly shows that these surfaces form a central core, consisting of high density cells from both cell populations that is flanked on all





**Fig. 4.** Differential density scatter plots and isorelational surface mapping. (**A and B**) represent the spatial distribution of cholinergic (dots in panel **A**) and parvalbumin (dots in panel **B**) cells from the same brain showed separately. Filled circles mark the high density locations where the density of cholinergic or parvalbumin cells is higher than 15 cells in the unit space ( $250 \times 250 \times 50 \mu\text{m}$ ). (**C**) The scatter plots of both cholinergic (red in the color version of this figure) and parvalbumin (green) cells are superimposed on the isorelational surface (dark solid area; violet in the CD-ROM file) where the density of both the cholinergic and parvalbumin cells is  $>5$  and the ratio of cholinergic–parvalbumin cells is at least 0.5 or higher. (**D**) Merging the cholinergic–parvalbumin, cholinergic–calbindin, and cholinergic–calretinin isorelational surfaces (using cell density  $\geq 5$  in the unit space) into one scheme reveals that the cholinergic “column” can be parcellated into clusters of different sizes. Different shading of surfaces cover the spaces where the relationship of cholinergic cells to parvalbumin (green in the color version), calretinin (yellow), and calbindin (blue) neurons is similar (0.5 or higher). A color version of this figure is enclosed in the CD-ROM.

sides with single-cell populations of gradually decreasing densities (Fig. 4C). Merging the three pairwise isorelational surfaces (cholinergic–parvalbumin, cholinergic–calretinin, and cholinergic–calbindin) into one scheme suggests that the cholinergic cell “column” can be parcellated into several smaller clusters or larger amalgamations, in which cholinergic cells are mixed with the other three cell types in a specific fashion



(Fig. 4D). Using a section-by-section analysis of the overlap, as shown in Figures 2C and D, one can get a fairly good idea about the composition of the mixed clusters. The advantage of the combined 3D isorelational surface rendering of Figure 4D is indeed in the totality of this image. Comparing similar types of renderings from different brains, a similar global pattern emerges suggesting that the configuration of the isorelational surfaces is not by chance and that the high density clusters in the individual cell populations may correspond to the zones where the different cell populations overlap with each other. The location of these overlapping zones may be determined during ontogenesis.

#### 9.4. CHOLINERGIC CELL GROUPS SHOW REGIONALLY SELECTIVE DENDRITIC ORIENTATION

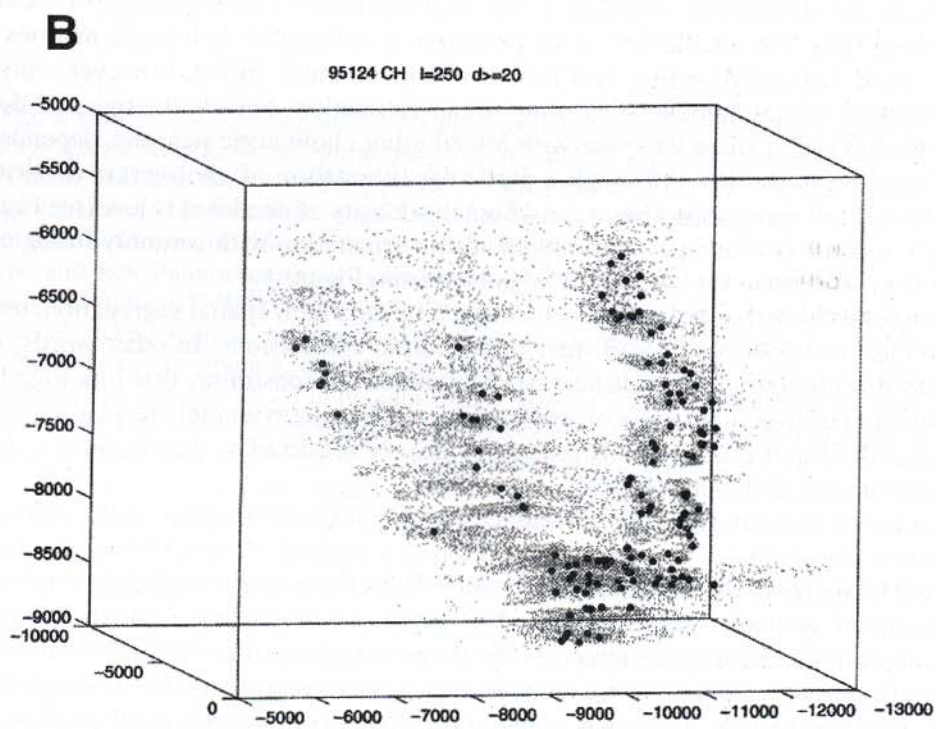
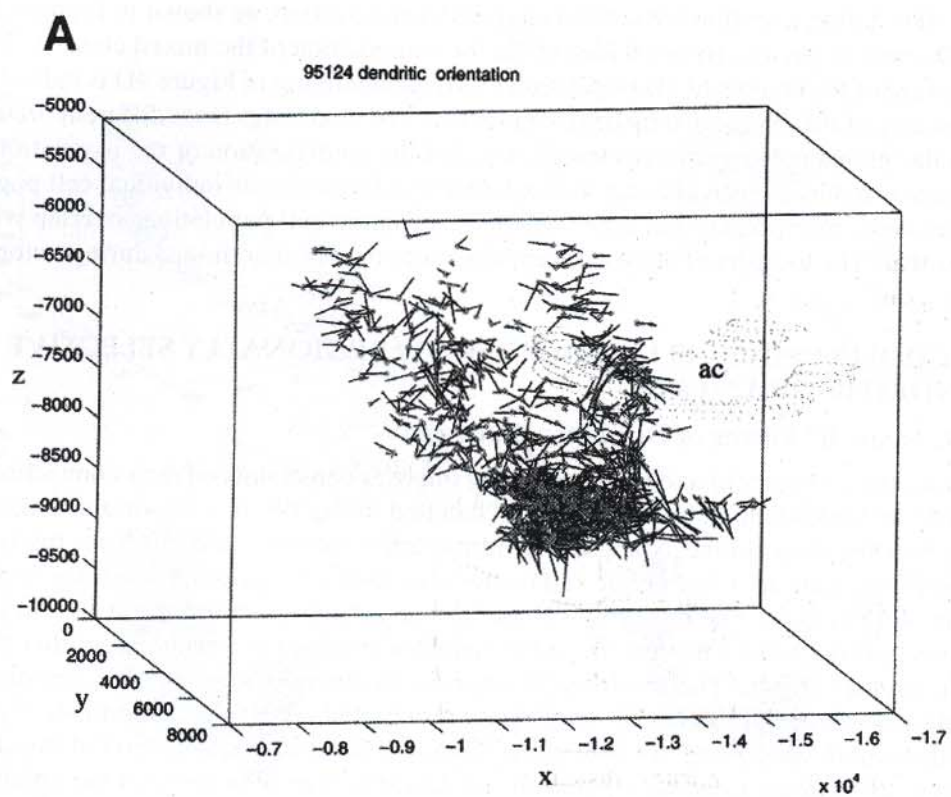
##### 9.4.1. Mean 3D Vector of Dendritic Processes

Since the geometry of axons and dendrites imposes constraints on their connections, in order to understand how information is handled in the BF, it is important to determine how the shape of the axonal and dendritic arborizations could influence regional connectivity patterns. Cholinergic cell bodies give rise to 2–5 primary dendrites radiating in all directions. The relatively straight primary dendrites bifurcate in an iterative fashion, and the sum of the lengths of the daughter branches is usually larger than that of the mother branch. The dendrites of adjacent cholinergic neurons often constitute overlapping fields. The dendrites are freely intermingled with passing myelinated fiber bundles within which they are embedded. Thus, the dendritic organization of the cholinergic BF neurons resembles that of the isodendritic type of neurons of the reticular formation (42–44) or the so-called interstitial neurons characterized by Das and Kreutzberg (45). The total length of the dendrites of individual cholinergic neurons in rats is about 4 mm, arborizing in a box of about  $0.1 \text{ mm}^3$ , filling, however, only a fraction of its spatial domain. According to our estimation, one cholinergic cell dendritic domain might share its space with 50–80 other cholinergic neurons, depending on its location in the BF. Although a particular orientation of cholinergic dendrites could be noticed upon inspecting areas where the density of dendrites is low (see Fig. 1 in [46]), it is not possible to appreciate dendritic orientation with certainty in regions where the cell density is high, as can be judged from Figure 1.

We assumed that the cholinergic cell clusters, beyond their spatial segregation, must fit into the functional network of their input–output connections. In other words, we assumed that cholinergic cell clusters develop under the constraints that link together functionally related output (neocortical) and input (brainstem and telencephalic) pathways, and this input selectivity, we reasoned, must be reflected by the anisotropic dendritic orientation of the putative cell clusters.

In order to correlate regional differences of dendritic orientation to the spatially distributed population of neurons, we developed a method of representing the main dendritic branches of individual neurons with 3-D vectors and embedded them into the 3D coordinate system of the cell bodies. The origin of a vector represents the position of the neuron, its orientation represents the dominant orientation of the dendritic tree (for details, see Appendix 9.9.4.), and the length of vector represents the average length of the dendritic branch. The main orientation vectors of 750 individual cholinergic







cells, selected from a population of about 15,700 cholinergic cells, are shown in Figure 5A. Rotation and navigation in the 3D plot made it possible to gain insight into the vector orientation even in the denser cell clusters. Comparison of Figure 5A with the differential density scatter plot of the same dataset, shown in Figure 5B, suggests a tendency of iso-orientation of dendrites within a given cholinergic cell cluster.

#### 9.4.2. 2D Dendritic Stick Analysis (Polar Histogram)

To obtain a quick qualitative characterization of the directional distribution of dendritic growth projected onto the plane of sectioning, the polar histogram is the method of choice (NeuroLucida® software package; see also Appendix 9.9.4. and [47]). In essence, using only the x and y coordinates of the traced dendritic segments, where individual segments are composed of pairs of adjacent points, the algorithm pools together all the segments around a center but preserves their length. The total range of angles is then binned to equal sectors, and the program calculates the sum of segments in each bin. The radial length of a filled sector is proportional to the total length of the dendritic branches of that specific orientation, thus the contributions of segment lengths and segment counts of that specific orientation are inseparable. In other words, a few long segments can add up to the length of many short dendrites. Depending on the choice of binning interval, the angle discrimination can be finer or broader. Analyzing BF cholinergic dendritic orientation by polar histograms suggests a regional orientation preference (Zaborszky, Nadasdy, and Somogyi, in preparation).

In contrast with the polar histogram method, the vector representation preserves the neuronal identity of dendrites, instead of pooling them together, and still provides an overall view of orientation of dendrites. The main advantage, however, is that vectors relate the dendrites to the spatial distribution of the neurons in a simplified and meaningful fashion. To compare the regional dendritic orientation derived from polar histograms with the orientation vectors calculated for individual cells, we selected a subspace of the septal area where a more detailed analysis of subpopulations of cholinergic neurons was available. The NeuroLucida program allows one to outline and select cell populations from any number of sections in a series and to construct a polar histogram of the dendrites pooled together from the selected cell populations. Figure 6A represents a portion of the septal area from Figure 5A viewed from a sagittal direction. Figure 6B displays cholinergic cells whose dendrites were traced from a series of sections cut in the sagittal plane. The selection areas of the four polar histograms of Figure 6C–F are indicated by boxes of various sizes in the upper right diagram. Comparing the dendritic orientation obtained from the polar histograms of pooled dendrites with the mean 3D vector of the dendritic branches indeed suggests that subpopulations of

**Fig. 5. (facing page) (A)** Mean orientation of dendritic branches. The initial segments of dendrites are represented by dots. The outlines of the anterior commissure (ac) are indicated by small dots. **(B)** Differential density scatter plot of the same database. Dots represent cholinergic cells ( $n = 15,700$ ), filled circles mark the high density locations where the density of cells is  $\geq 20$  per unit space ( $250 \times 250 \times 100 \mu\text{m}$ ). Flakes are due to the section steps along the z axis. Cells and their dendrites were mapped from 34 consecutive horizontal sections stained for choline acetyltransferase. The comparison of panels **A** and **B** suggests the iso-orientation of dendrites in the high density cell cluster. A color version of this figure is enclosed in the CD-ROM.



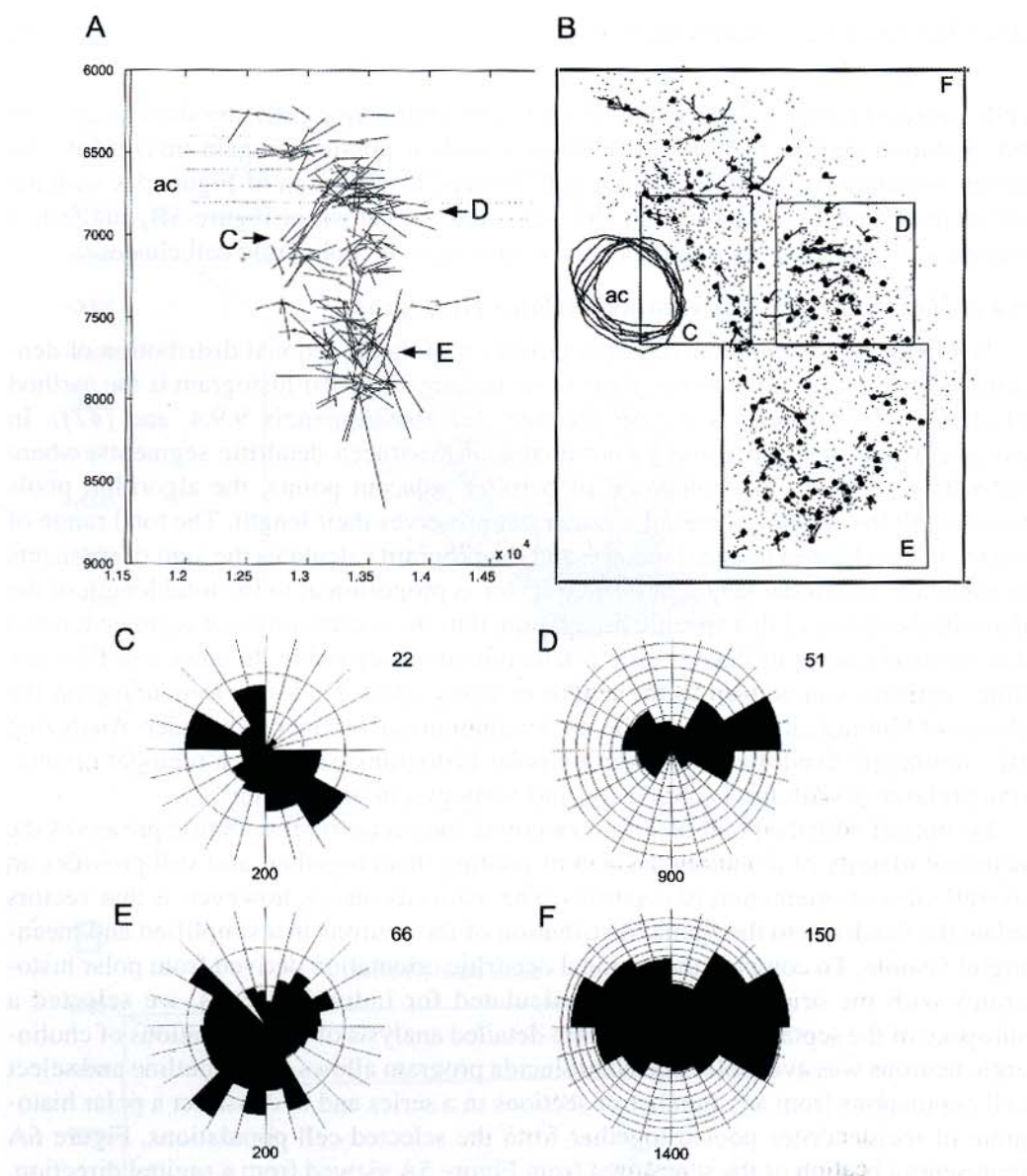


**Fig. 6.** Comparison of the dendritic orientation derived from polar histograms with the orientation vectors. (A) Part of the septal area from Figure 5A as viewed from the sagittal direction. Letters C, D, and E with arrows point to regions that may correspond to the same cell populations as selected for the polar histograms from sagittal sections of a different brain as shown in panel B. (B) Cholinergic cells (137) (filled circles) were selected from a stack of sagittal sections comprising the septal region ( $n = 2266$  cholinergic cells, dots) for dendritic tracing. Letters C, D, E, and F mark boxes that were used to select dendrites for the orientation analysis. In both panels A and B, ac indicates the location of the anterior commissure. Despite slightly different orientation of the sagittal sections, one can recognize the same cell groups as seen in the 3D rendering. (C–F) Polar histograms representing dendritic orientation from indicated areas. Numbers at upper right indicate the number of dendritic segments in the sample. Numbers along the circles within the polar histograms mark distances in micrometers from the origin (see section 9.9. for explanation). A color version of this figure is enclosed in the CD-ROM.

cholinergic cells can be delineated based upon their density and main orientation of their dendritic arbor. Therefore, one of the key features of cluster organization is the iso-orientation of their dendrites.

### 9.5. VARIOUS AFFERENTS IN THE BF SHOW REGIONALLY RESTRICTED LOCALIZATION

Using a double strategy of recording the location of putative contact sites between identified axons and cholinergic profiles as well as identifying in representative cases under the electron microscope the presence of synapses, one can get a fairly good idea about the extent of potential transmitter interactions in the BF (for references, see [4,38]). Although the noradrenergic and dopaminergic axons contact cholinergic neurons in extensive portions of the BF, the majority of afferents (cortical, amygdaloid, striatal, peptidergic) appear to have a preferential distribution in the BF; thus a specific input can contact only a subset of neurons. Figure 7 gives examples of the distribution of restricted vs more diffuse afferents.

### 9.6. PROBABILITY OF CONNECTIONS

In many cases examined, labeled terminal varicosities detected in the BF were related to both cholinergic and noncholinergic postsynaptic elements. In fact, the detectability of synapses on cholinergic neurons was usually proportional to the density of terminals present in a given area. Thus, at first approximation, the probability of synapses between cholinergic neurons and various afferents may depend on the geometry of the dendritic arbor and axonal ramifications. Since a systematic study comparing the dendritic arbor of cholinergic neurons with various afferent orientations would require a substantial time, we only briefly comment on this issue here, by documenting the case of calcitonin-gene-related-peptide (CGRP)-containing axons in the internal capsule. Figure 8A shows cholinergic cells and their traced dendrites at about 1.5 mm posterior to bregma. Figure 8B is a schematic drawing from an adjacent section that was immunostained for CGRP and whose axons in the internal capsule were traced at high magnification. Comparing the polar histograms of cholinergic dendritic trees in the internal capsule (Fig. 8C) with that of CGRP axons (Fig. 8D), it is obvious that CGRP axonal ramifications have the same prevailing direction as the dendritic arbor of cholinergic neurons. Indeed, electron microscopic studies confirmed abundant presence of CGRP in axon terminals synapsing with cholinergic neurons in this region (48).

The probability of synaptic connections can be calculated from the overlap of axonal and dendritic domains (49). The probability of having more than one synapse between any given presynaptic axon and a postsynaptic cell is maximal in the case when the terminal axon and the receiving dendrite are running in parallel ("climbing" fiber type contact). However, only one synapse is possible if the axon runs at right angles to the dendrite ("crossing over" type of geometry). If the terminal axon is oriented obliquely to the receiving dendrite, the probability of synaptic contacts is a cosine function of the angle between the axon and the dendrite (50). Since various afferents show specific localization, it is likely that cholinergic cells in various BF subdivisions can sample a unique combination of afferents. It seems that in each major subdivision of the BF along the axis of the major orientation of the cell bodies, a specific type of axon is



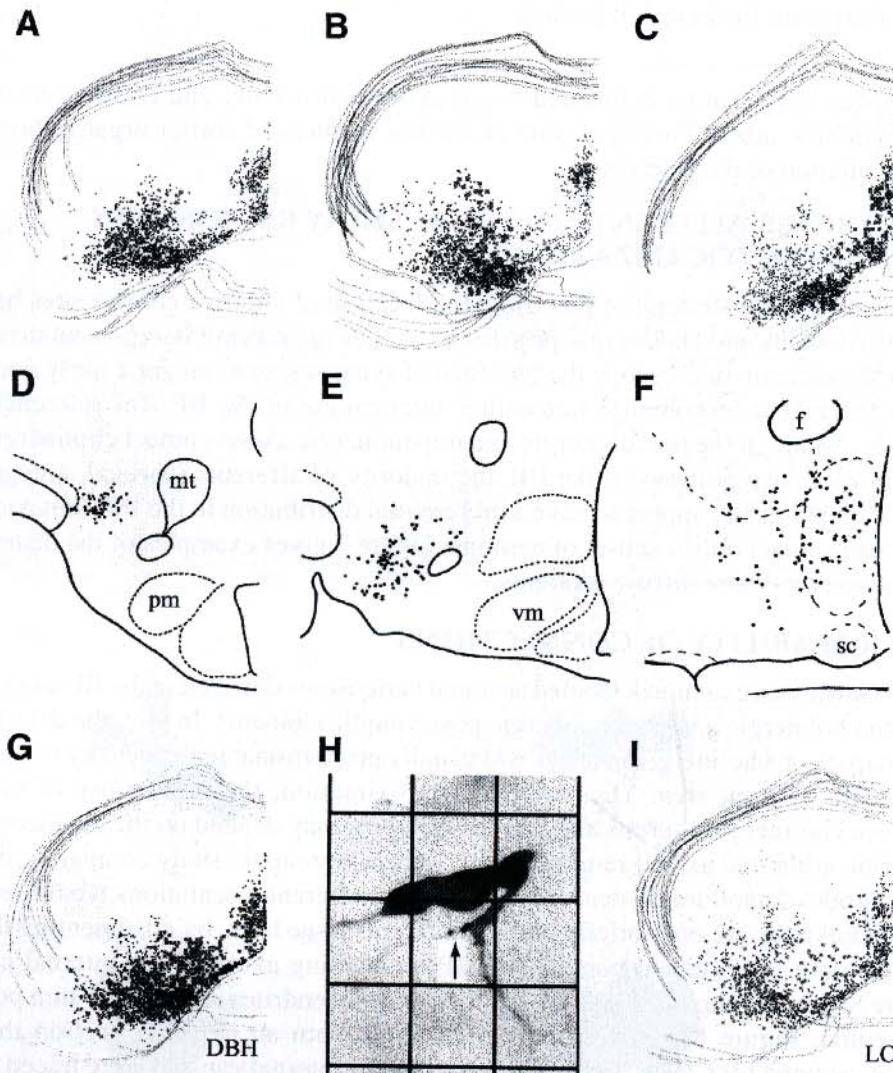


**Fig. 7.** Differential distribution of various afferents in the cholinergic forebrain. (**A–C,G,I**) Composite maps illustrating putative zones of contacts between afferent fibers and cholinergic neuronal elements following *Phaseolus vulgaris* leucoagglutinin (PHA-L) injections into the (**A**) far-lateral hypothalamus, (**B**) midlateral hypothalamus, (**C**) medial hypothalamus, (**I**) locus coeruleus. (**G**) Shows the distribution of putative contact sites from a material stained for dopamine- $\beta$ -hydroxylase and choline acetyltransferase. (**H**) PHA-L-labeled terminal varicosities (arrow) in close apposition to a proximal dendrite of a cholinergic neuron. The grid simulates the ocular reticle used to screen sections for high magnification (63 $\times$ ) light microscopic analysis. One division of the grid = 16  $\mu$ m. Cholinergic neurons are represented by dots. Zones of putative contacts between cholinergic elements and terminal varicosities are depicted as solid squares (corresponding to 80  $\times$  80  $\mu$ m areas in the section). (**D–F**) Location of labeled cells at the PHA-L injection sites from cases depicted in panels **A–C**. Panels **A–C,H** are modified from Cullinan and Zaborszky (57) with kind permission from Wiley-Liss. Panels **G** and **I** are modified from Zaborszky et al. (51), with permission from Elsevier Science. A color version of this figure is enclosed in the CD-ROM.

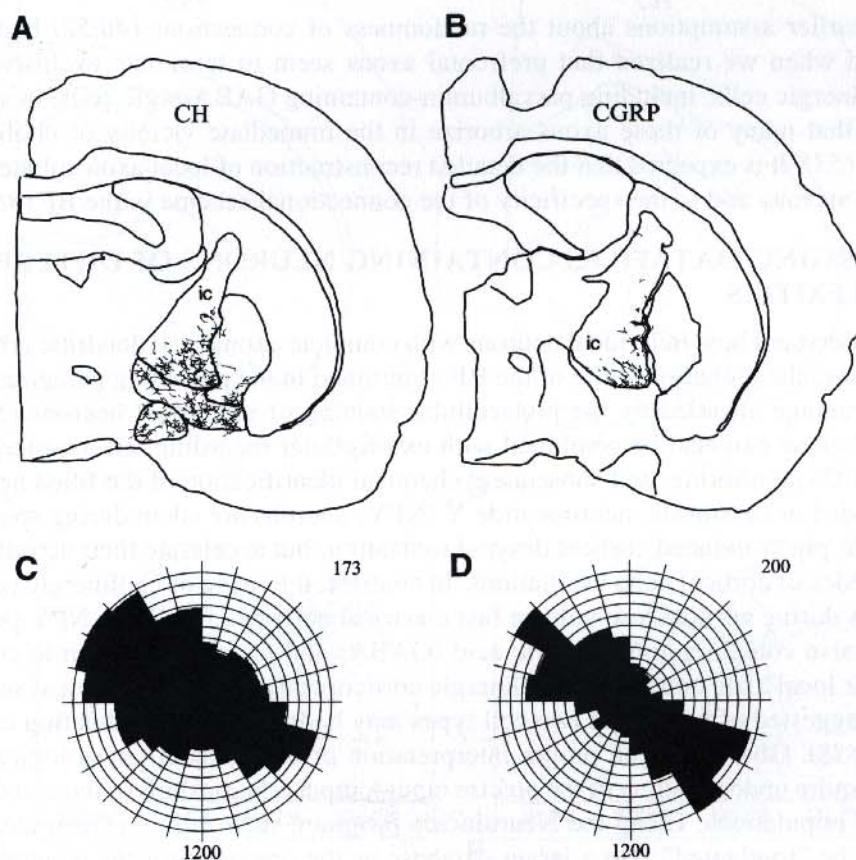


**Fig. 8.** Comparison of the 2D orientation of cholinergic dendritic segments (**A**) and CGRP-containing axons (**B**) in the internal capsule (ic). (**C and D**) Polar histograms of cholinergic dendrites (**C**) and CGRP axonal ramifications (**D**) from the same general area. Note that the majority of dendrites and axons occupy the same sector of the polar histograms. Upper right numbers indicate the number of segments in the analysis. The outer circle of the polar histogram correspond to a 1200- $\mu$ m diameter around the origin.

maximally aligned with the preferred orientation of cholinergic dendrites of that area. Different cells, or perhaps different dendrites of the same cell, can sample the same input differently according to the spatial organization of the dendrites and corresponding axons. For example, the majority of dopamine- $\beta$ -hydroxylase positive varicosities (used to stain noradrenaline and adrenaline containing neurons) establish single synapses with cholinergic dendrites, while a small population of cholinergic neurons (at most 5%) appears to receive multiple contacts on their dendrites in the form of climbing-type arrangements. Such climbing-type synapses were most often detected in the substantia innominata (Fig. 3 in [51]), but were also occasionally seen in other BF regions. It is unclear whether cholinergic neurons with climbing-type inputs are different in other respects, however, one can speculate that the noradrenaline released at these climbing-type synapses must have a more powerful action on these selected neurons as compared to the single synapses at random locations.



Our earlier assumptions about the randomness of connections (46,52) had to be modified when we realized that prefrontal axons seem to terminate exclusively on noncholinergic cells, including parvalbumin-containing GABA-ergic cells, in spite of the fact that many of these axons arborize in the immediate vicinity of cholinergic neurons (53). It is expected that the detailed reconstruction of local axon collaterals of BF neurons may add to the specificity of the connectional scheme in the BF (38).

### 9.7. MERGING DATAFILES CONTAINING NEURONS OF DIFFERENT COMPLEXITIES

To understand how individual neurons with complete axonal and dendritic arborizations fit into the global structure of the BF as outlined in the preceding paragraphs, we took advantage afforded by the juxtacellular staining of individual neurons (54,55). This technique can also be combined with extracellular recording, electroencephalogram (EEG) monitoring, and subsequent chemical identification of the filled neurons. As recorded in anesthesia, neuropeptide Y (NPY) neurons are silent during spontaneous or tail pinch-induced cortical desynchronization, but accelerate their activity during episodes of cortical delta oscillations. In contrast, the firing of cholinergic neurons increases during cortical low-voltage fast electrical activity (55). Since NPY-positive neurons also contain  $\gamma$ -aminobutyric acid (GABA) and have been shown to contact, with their local axon collaterals, cholinergic corticopetal cells, a hypothetical scenario can be suggested of how these two cell types may be involved in modulating cortical activity (38). Obviously, the proper interpretation of these electrophysiological data would require understanding of the precise input-output relationships of these and other neuronal populations. Using the Neurolucida program, such fully reconstructed neurons can be "implanted" into a larger database as the one used for the generation of Figure 4; thus individual electrophysiologically and chemically identified neurons can virtually be placed into their natural environment. In this way a functional property such as "content" can be placed into the anatomical maps as "context". Figure 9C and D display a locally arborizing NPY neuron and a cortically projecting and also locally arborizing cholinergic neuron, respectively. Although both of these neurons are located (Fig. 9A,B) in the same general BF area (horizontal limb of the diagonal band), their local axons may contact different postsynaptic target, and similarly, their dendrites should sample, at least in quantitative terms, different inputs. According to our estimations, this particular cholinergic neuron gives rise to about 1400 local axonal varicosities, and in the space defined by its axonal arbor, there are approximately 1500 cells. On the other hand, the NPY neuron presented here distributes about 2900 varicosities in a space that contains 1250 neurons. Whether or not these varicosities represent synapses and whether or not they address postsynaptic targets selectively, remains to be investigated.

### 9.8. CONCLUDING REMARKS

Since the seminal paper of Schwaber et al. (56), who first used computer-aided data acquisition and 3D reconstruction of BF cholinergic neurons, the progress in understanding the organization of the BF has been very slow. It is likely that, in the coming years, the sophisticated use of multi-electrode recordings in awake behaving animals

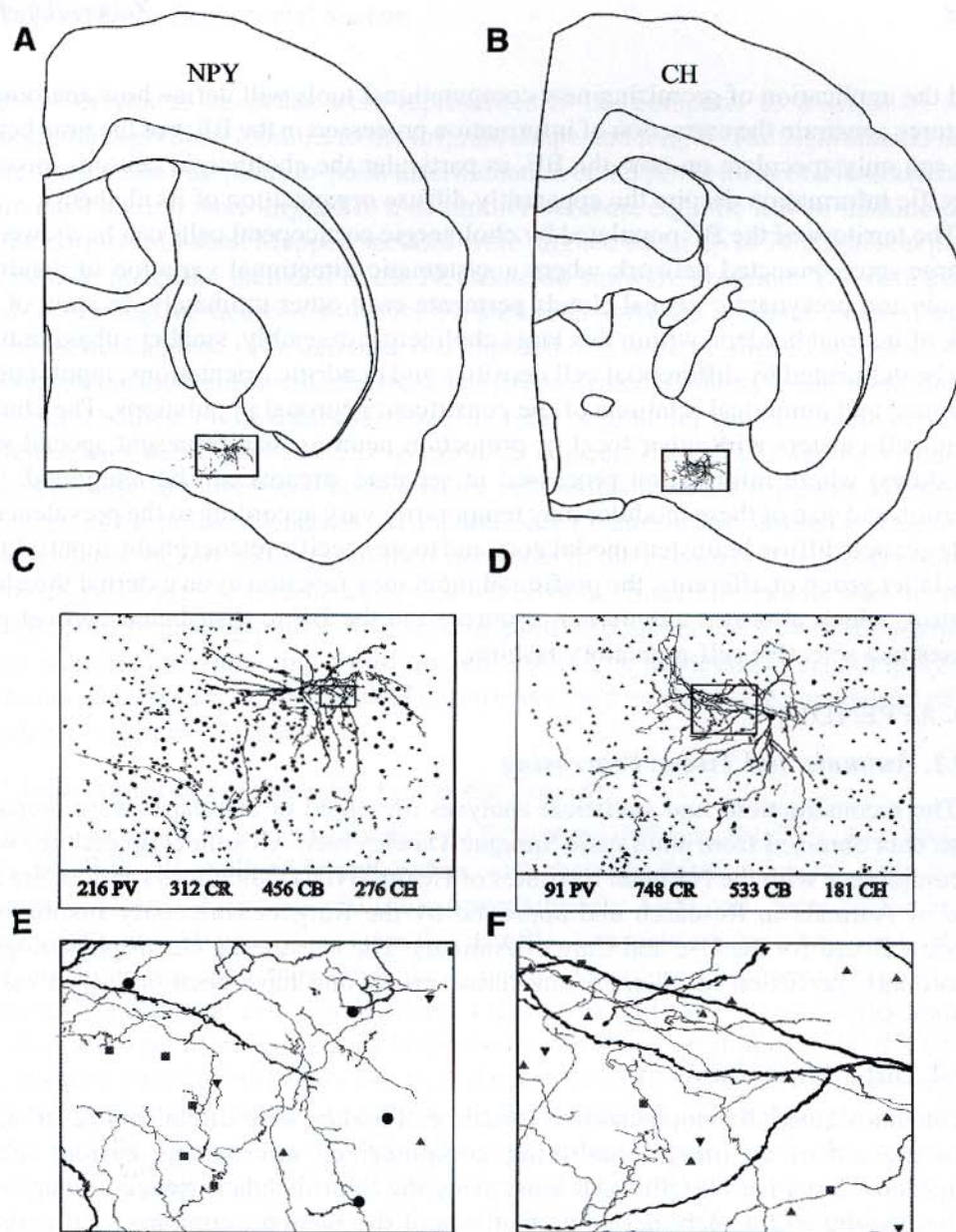


**Fig. 9.** Distribution of different cell types in the neighborhood of identified NPY (A,C,E) and cholinergic (B,D,F) neurons. (A and B) Schematic drawings illustrating the location of the electrophysiologically and chemically identified neurons. (C and D) Coronal view of the identified neurons embedded into the same general region of the BF derived from a different database that contains four different cell populations. Filled circles, parvalbumin; up triangles, calretinin; down triangles, calbindin; squares, cholinergic neurons. The approximate number of cell bodies from each cell population that can be found in the 3D volume of the single-cell axonal arbor is indicated below. (E and F) Enlarged view of the boxes from panels C and D. Thicker black indicates dendritic processes, and thinner lines indicate axonal ramifications. Note that the small varicosities along the axonal collaterals correspond to putative synaptic boutons. A color version of this figure is enclosed in the CD-ROM.



and the application of promising new computational tools will define how anatomical features constrain the extraction of information processed in the BF. For the time being, we can only speculate on how the BF, in particular the cholinergic neurons, process specific information despite the apparently diffuse organization of its elements.

The territory of the BF populated by cholinergic corticopetal cells can be viewed as a large interconnected network where a systematic directional variation of dendritic clouds and presynaptic axonal clouds permeate each other intimately. In spite of the lack of internal borders, within this large cholinergic assembly, smaller subassemblies can be delineated by differential cell densities and dendritic orientations, input–output features, and numerical relations of the constituent neuronal populations. The cholinergic cell clusters with other local or projection neurons may represent special sites (modules) where information processed in separate streams can be integrated. The location and size of these modules may temporarily vary according to the prevalence of state-related diffuse brainstem modulatory and more specific telencephalic inputs. From this latter group of afferents, the prefrontal input may function as an external threshold control, which allocates attentional resources via the BF to distributed cortical processes in a selective self-regulatory fashion.

## 9.9. APPENDIX

### 9.9.1. *Animals and Tissue Processing*

The reconstructions and statistical analyses presented in this paper were prepared from data obtained from adult male Sprague-Dawley rats. All animal procedures were in compliance with the National Institutes of Health (NIH) Guidelines for the Care and Use of Animals in Research and approved by the Rutgers University Institutional Review Board for the Use and Care of Animals. The anesthesia, electrophysiological recordings, perfusion of animals, and tissue processing have been described earlier (55,57–58).

### 9.9.2. *Data Acquisition*

Immunostained diaminobenzidine-labeled cell bodies were digitalized in BF areas with the aid of an image-combining computerized microscope system (Zeiss Axioscope, 20× Plan-NEOFLUAR lens) using the Neurolucida software package (59) (MicroBrightField, Colchester, VT). Outlines of the sections, contours of structures, and fiducial markers were drawn with a 5× Plan-NEOFLUAR lens. Dendritic branches were traced from the cell body by connecting tracing points by straight lines (Plan-APOCHROMAT 40× (NA = 1.0) or Plan-NEOFLUAR 63× (NA = 1.25) oil immersion lenses). Sections containing fluorescent-tagged cell bodies were mapped by using the epifluorescent setup of the Axioscope microscope equipped with appropriate filters. Fast Blue and Fluor-Gold-labeled projection neurons (exciter/barrier filter set 365/418) and the fluorescein isothiocyanate (FITC)-labeled (FITC exciter/barrier filter set 450–490/520) cholinergic cells could be separately visualized in the same section. Labeled cells were mapped from every 8<sup>th</sup> sections at a magnification of 20×.

Although the outlines, and contours were drawn flat, disabling z input information, dendrites were followed in the depth of the sections (50 or 100  $\mu$ m) by changing the



focus. Curvilinear dendrites were represented in the computer as a series of short straight lines giving a close fit to the original shape and length. The Neurolucida hardware system allows a point-to-point discrimination of  $0.3\text{ }\mu\text{m}$  in all axes. Neurons traced from each section were aligned to a common reference, e.g., the lowest midline point of the corpus callosum. Mapped sections were aligned using up to 99 alignment points for best-fit matching included in the Neurolucida software program. The data generated by tracing the neurons using the Neurolucida software are later referred as the Neurolucida database. The database is composed of a stack of aligned sections.

Neurons in the Neurolucida database were represented by the x, y, and z coordinates of the cell bodies. In the database, dendritic trees originating from the same neuron at different sites were represented as separate but adjacent data blocks and were encoded independently from their cell bodies. Since cell bodies were not traced as 3D objects, the origin of the primary dendrites did not necessarily match in any dimension. Due to this independence of cell bodies from their dendrites in the encoding scheme, finding the common cell body for each dendrite was not obvious. Branching points were marked. Based on the branching points, first, second, third, and higher order dendritic segments were identified as stemming from a parent node. The hierarchical encoding system (introduced by Neurolucida) allowed us to recursively represent the complexity of any dendritic tree in the database.

### 9.9.3. Selection of Neurons for Dendritic Tracing

In this paper, dendritic data are derived from three different datafiles. As a preliminary material, all cholinergic cell bodies with their dendritic processes were traced from seven coronal sections ( $50\text{ }\mu\text{m}$ ). Approximately 1300 cells were traced in this material. Figures 1B and 8A are from this datafile. To create a more complete database, a second brain was cut in horizontal planes into 34 consecutive sections ( $100\text{ }\mu\text{m}$  thick), and every cholinergic cell was digitized. Figures 5A and 6A are generated using this horizontal dataset. Finally, a third brain was cut in the sagittal plane ( $100\text{ }\mu\text{m}$  thick), and the data presented in Figure 6B–F are derived from the septal region of this sagittal dataset. In this latter brain, similarly to the horizontal set, all cholinergic cell bodies were digitized. From the horizontal and sagittal dataset, about 5% of the total cholinergic neurons were selected for dendritic reconstruction based on a random sampling of the total population. In order to obtain a sample of neurons representative of the inhomogeneous distribution of the entire population, we used a combination of two different density criteria, one with high and another with low resolution. For both selections, the space that incorporated all cholinergic cells was subdivided into subspaces of identical size (voxels or unit spaces), and on these voxels, based on the cell density, different selection criteria were applied. As for a high density criterion, we selected cells from voxels of  $100 \times 100\text{ }\mu\text{m} \times$  section thickness ( $=100\text{ }\mu\text{m}$ ). To resolve a larger scale inhomogeneity, cells were selected from voxels of  $500 \times 500\text{ }\mu\text{m} \times$  section thickness. The larger voxel captured the density differences at a  $500\text{ }\mu\text{m}$  resolution. The  $100\text{-}\mu\text{m}$  sample size was applied to sample local densities at a  $100\text{-}\mu\text{m}$  scale. Next, the two samples were combined. As a result, the combination of samples reflected both the global and the local distribution features of the cells. From each voxel, where the



local cell counts met the density criteria, a neuron was selected on a random basis and marked for dendritic tracing. The number of cells,  $s$  selected for dendritic tracing from each voxel with both  $v'$  and  $v''$  sizes was proportional to the natural logarithm of the number of cells,  $n$  within the given space,  $v_{ijk}$ , multiplied by a constant,  $c$  as follows:

$$s = c \times [\log(n_{v'ijk}) + \log(n_{v''ijk})]$$

For the interpretation of  $i$ ,  $j$ , and  $k$  voxel indices, see (41). The purpose of the multiplication factor  $c$  was to provide flexibility to scale up or down the number of selected cells. The value of  $c$  was set to 0.5 with 100  $\mu\text{m}$  grids and 0.4 with 500  $\mu\text{m}$  grids. The edges of the two voxel types  $v'$  and  $v''$  were 100  $\mu\text{m}$  and 500  $\mu\text{m}$ , respectively. Technically, the datafile of traced cell bodies was exported from Neurolucida, parsed for different objects (cell bodies, structure outlines, etc.), and the point coordinates of cell bodies were extracted. A custom written C++ program performed the partitioning, cell counting, and selection of target cells for dendritic tracing. With this sampling scheme, we marked 750 cells from the horizontal dataset ( $n = 15,776$ ) and 137 from the septal sagittal dataset ( $n = 2266$ ). The generated data file with the target cells marked, was inserted to the original Neurolucida datafile for subsequent dendritic tracing.

#### 9.9.4. Analysis of the Data

For data analysis, as described here, we extracted the  $x$ ,  $y$ , and  $z$  coordinates of the cell bodies from the Neurolucida database and saved them in ASCII format, each cell type in different data files. Structure outlines were stored separately. The medial, lateral, dorsal, and ventral extremes of the cholinergic cell distribution were taken as a 3D framework to incorporate the entire database. For expressing regional density changes, the 3D framework was subdivided into virtual blocks of identical size denoted as "voxels". Section thickness served as unit size for the  $z$  dimension. If cells of different types were mapped from different but adjacent sections (plots in Figs. 4 and 9C,D), then their  $z$  coordinates were collapsed into a common 2D plane (master plane) by removing the within-section depth coordinates, but preserving the  $x$  and  $y$  coordinate of the cells. Each different cell type was separately counted in each of these master plane lattices. For visualization, we used different thresholds. Differences in the voxel size and thresholding could significantly influence the obtained results. A more detailed methodological description and discussion is given in a recent publication (41).

*Differential density 3D scatter plot.* Density differences within or between cell populations can be represented in 2D isodensity maps (60). The obvious limitations of this method is the lack of the third dimension. Our method (41) quantifies density differences first, then plots the density descriptors in a real 3D coordinate system. The input data is provided as position of cell bodies by their locations as points in the 3D Euclidean space. In this database, each row represents a single cell given by the  $x$ ,  $y$ , and  $z$  coordinates relative to a reference point as the origin. The entire database is placed into a framework, which is partitioned into boxes of identical size (voxel) as a grid system. Cells are counted within each voxel. In contrast to the parametric representation of the space, this provides a 3D volumetric dataset where the dimensions are the  $x$ ,  $y$ , and  $z$  position of the voxel and the local cell count within the voxel space. Voxels of cell



counts larger than a predefined density are considered and represented by a single marker randomly selected from the neurons in the corresponding voxel. The distribution of these markers highlights locations where high density neuronal clusters occur. Figures 4A,B and 5B represent this type of analysis.

*Isodensity surface mapping.* The spatial distribution of different cell types may be very complicated as neuronal populations interdigitate, intersect, or overlap with one another. Instead of using scatter plots, the spatial organization of density differences is better visualized by rendering a surface around large density cell groups, especially when multiple cell types are concerned. Similar to the "differential-density 3D scatter plot," a selected set of voxels are visualized. However, instead of representing them by single points, the algorithm renders a surface around voxels of larger than certain cellular density. The procedure of subdividing the 3D database into voxels (unit spaces) and calculating the voxel cell densities is identical to that of the "differential-density scatter plot." Conversion of the 3D point-coordinate database, where the entries are the cells, to a density data constructs a volumetric database. In the volumetric data, the entries are voxels defined by their 3 coordinates and the associated cell densities. Then, a density threshold is defined, and voxels characterized by larger density than the threshold are identified. The algorithm renders a 3D skeleton and determines a 2D manifold on the skeleton that is defined by interconnecting points that separate the higher density space from a lower density space. The manifold is further partitioned onto triangles and surface elements are rendered to each of these triangles. These surface elements are then smoothed, and reflectance property as well as light source are defined. For surface rendering, the C++ program and the 3D visualization toolbox of Matlab R11® (MathWorks, Inc.) were used. Figure 3B was generated by this method.

*Isorelational surface rendering.* Similar to the "isorelational scatter plot", the aim of this representation is to show the codistributive association between different cell types or other variables. In contrast to the "isorelational scatter plot", this plot renders a surface around the population of cells where certain density ratio is detected. Since the association of different cell types have a typically complicated spatial configuration, the scatter plot of neuronal markers does not reveal the true 3D structure. In order to reduce the complexity, voxels, where a certain density ratio of two cell types is established, are rendered with a surface. This surface separates cells where certain density ratio is higher than a critical value. The unique feature of the "isorelational surface rendering" method is the visual representation of abstract relationships, which is more important for understanding functional connections between neurons than exact locations of cell bodies. Technically, the 3D database of cell bodies is subdivided into unit spaces for both cell types. Then cell density ratios are calculated within each unit space (voxel) shared between the two cell types. The density ratios are arranged in a 3D matrix containing various ratios. Isodensity demarcation lines are calculated and rendered by a surface in such a way that cell bodies with density ratios larger than a specific number are covered by the surface. Density ratios smaller than the critical one are located outside of the surface. For visualization purposes, a range of critical density values must be applied for testing the integrity of clouds and to make sure that there are no hollow spaces covered. The algorithm of surface rendering is the same as the one described at the "isodensity surface mapping". Complex relationships between mul-



multiple components such as density relations of multiple cell types can be decomposed into pairwise relations and visualized as merged surfaces. Color coding of surfaces of different cell types helps to interpret complicated arrangements. The plots in Figure 4C,D were generated according to this method. A more detailed description of the methods described so far in this section is given elsewhere (41).

**Mean 3D vector of dendritic processes.** Individual dendritic branches may have a principal orientation adapted to making contacts with also oriented axons, independent from the orientation of dendritic mass. To test this, the principal orientation of dendritic branches was expressed by the mean branch orientation and approximated by the average orientation and average length of the dendritic tree. The orientation and length were combined into a  $V_{(P_0, P_1)}$  vector originating from the point  $P(x_0, y_0, z_0)_i$ , where the dendrite stemmed from the cell body and pointing to the  $P(x_1, y_1, z_1)_i$  point, which represented the average length and orientation. In this analysis, we first calculate the  $dx_i$ ,  $dy_i$ , and  $dz_i$  vectors as Euclidean distances between adjacent branch points, and the average of the  $dx_i$ ,  $dy_i$ , and  $dz_i$  is used as a single vector to represent the main orientation tendency of the dendrite. Since multiple origins of dendritic processes were possible, the orientation vector was calculated separately for each main branch resulting in different vectors per cells originating from nearby points. Parsing of the Neurolucida data files and computation of vectors was all carried out by custom written C++ codes and compiled for Silicon Graphics and Pentium class computers using Irix and Linux operating systems, respectively. For visualization purposes, vectors were rescaled by a common multiplicative factor that made it easier to appreciate the main tendency of orientation. 3D aspects of the vector space were constructed by superposition of the vectors on the structure outlines (such as anterior commissure). Rotation and navigation in the database using Matlab 3D graphical user interface made it possible to gain insights of the vector orientation in the denser cell clusters. This type of analytical tool was applied to generate Figures 5A and 6A.

**2D orientation of dendritic processes.** The algorithm (polar histogram) supplied in the Neurolucida software package is similar to the analysis described by McMullen et al. (47). The difference is that in our case, the results are collected by a computerized system, and the artifacts of that collection process need to be filtered out. The algorithm for polar histogram breaks up the dendritic processes into line segments and determines the directions that these line segments point to and that of the lengths of these segments. The sum of the lengths of the small line segments is approx the same as the length of the original tracing. The direction of the vector is calculated by projecting the line segment onto the plane of the sectioning. This is accomplished with the arc-cosine function. The histogram represents the total length by the distance from the origin and an angle ( $\theta$ ) that the vector makes with the x axis plotted in the radial direction. Each sector in the polar histogram is the sum of all the dendritic growth in that particular range of angle. There is a unique value of the polar histogram for each value of the angle  $\theta$ . Some information has been lost because the dendrites that are traced in the sectioning plane are always going to be longer than dendrites in the plane perpendicular to the sectioning plane. Therefore, this type of analysis is useful primarily to characterize the orientation of dendrites that are roughly coplanar. Neurolucida allowed us to



outline and select cell populations based on anatomical markers from single sections or a stack of sections and to construct a polar histogram of the dendrites pooled together from all the marked neurons.

*Comparison of 3D location of labeled cells from different brains.* After mapping labeled cell bodies, the Neurolucida files were transferred to a Silicon Graphics (Octane) workstation for further analysis and 3D visualization using the Micro3D (Oslo Research Park) program. In order to compare data from several brains with multiple retrograde tracer injections, each section was visually aligned to the corresponding map of a "master" brain with the aid of surface contours and fiducial markers, including the corpus callosum, anterior commissure, internal capsule, stria medullaris, stria terminalis, and the fornix. To create a maximum fit, an interactive procedure was used, including moving, rotation, and shrinkage corrections along the x, y, and z axes. To avoid gaps between sections in the visualizations, individual cells were randomized in a  $400 \times 400 \times 50$ - $\mu\text{m}$  space (z-spread). Figures 2 A,B and 3A were generated according to this procedure.

*Overlap analysis.* The degree of overlap between two neuronal populations was estimated by subdividing individual sections into an array of  $500 \times 500$   $\mu\text{m}$  voxels and counting the number of digitized coordinate pairs (cell) per voxel using a custom-made program similar to the one applied by Alloway et al. (40). To avoid analyzing areas with low density of cells, only voxels containing 3 or more cells were included. Voxels containing a defined number of "population 1" or "population 2" cells are dark gray (red in the color version) or light gray (blue in the color version), respectively, while voxels containing a similarly defined number or more cells of both categories (at least 3 of each) are labeled white. The number of differently labeled voxels are counted for each section and also summed across sections and used to estimate the percentage of overlapping voxels and also the percentage of a given cell population in the overlapping voxels. The charts in Figure 2C,D are from this material.

*Merging files containing cells of different complexities.* Figure 9 C,D were prepared merging two different datafiles: one derived from a series of sections containing four different cell populations in the BF using immunostaining for parvalbumin (PV), calretinin (CR), calbindin (CB), and choline acetyltransferase (CH) ("four marker" brain). The other file contained a single electrophysiologically and chemically identified neuron (NPY or CH) with its axonal ramifications and dendritic trees digitized from a series ( $n = 10$ – $100$ ) of 50- $\mu\text{m}$  thick sections.

The cell mapping and anatomical landmarks were extracted from the four marker brain, in which four series of alternate sections ( $n = 48$ ) were stained with antibodies against CH, PV, CR, and CB. The distance between two consecutive sections stained with identical markers was 300  $\mu\text{m}$ . Adjacent four sections containing markers for PV, CR, CB, and CH were aligned using standard anatomical landmarks (i.e., corpus callosum, lateral ventricle, fornix, thalamus, optic chiasm) and collapsed into a single section by removing the within section depth coordinates, but preserving the x and y coordinates of the cells, resulting in a 3D series of 2D layers. The distance from bregma of each of this composed layers was calculated using the average of the original four



sections. This way, we created a set of 12 layers, each containing four different cell populations with their original x and y coordinates. The same dataset was the basis for the analysis documented in Figure 4.

Reconstruction of single identified cells was achieved by routine procedures as described in the literature (for references, see [61]). Since the tissue sections contain only one stained neuron, all axonal and dendritic processes can be followed through a series of adjacent sections. After determining the distance from bregma of the single reconstructed cell body, the corresponding section from the four marker brain was merged into the section that contained the single identified cell body. The axonal arbor fields of the single identified cells were outlined, and the number and cell types that were enclosed were extracted from the Neurolucida database. Data from the cell marker and fractal analysis of the axon arbor was then used to estimate the approximate numbers and types of cells that may be embedded in the axonal ramification space of the single reconstructed cell and could come into contact with it.

## ACKNOWLEDGMENTS

The research summarized in this review was supported by NIH Grant No. NS23945 and IR25 GM60826 to L.Z. and A.D. We wish to thank Mr. Jack R. Glaser, President, MicroBrightField, Inc. and other staff members of his company with whom our interaction has been excellent over many years.

## REFERENCES

1. Dunnett SB, Fibiger HC. Role of forebrain cholinergic system in learning and memory: relevance to the cognitive deficits of aging and Alzheimer's dementia. *Progr Brain Res* 1993; **98**:413–420.
2. Everitt BJ, Robbins TW. Central cholinergic systems and cognition. *Annu Rev Psychol* 1997; **48**:649–684.
3. Heimer L, de Olmos J, Alheid GF, Zaborszky L. "Perestroika" in the basal forebrain; opening the border between neurology and psychiatry. *Progr Brain Res* 1991; **87**:109–165.
4. Zaborszky L, Pang K, Somogyi J, Nadasdy Z, Kallo I. The basal forebrain corticopetal system revisited. *Ann NY Acad Sci* 1999; **877**:339–367.
5. Jones BE, Muhlethaler M. Cholinergic and GABAergic neurons of the basal forebrain: role in cortical activation. In: *Handbook of Behavioral State Control—Cellular and Molecular Mechanisms* (Lydic R, Baghdoyan HA, eds.) CRC Press, New York, 1999, pp. 213–234.
6. de Lacalle S, Saper CB. The cholinergic system in the primate brain: Basal forebrain and pontine-tegmental cell groups. In: *Handbook of Chemical Neuroanatomy. The Primate Nervous System, Part I* (Bloom FE, Bjorklund A, Hokfelt T, eds.) Elsevier, New York, 1997, pp. 217–252.
7. Geula C, Mesulam MM. Cholinergic systems and related neuropathological predilection patterns in Alzheimer disease. In: *Alzheimer Disease* (Terry RD, Katzman R, Bick KL, eds.) Raven Press, New York, 1994, pp. 263–291.
8. Swaab DF. Neurobiology and neuropathology of the human hypothalamus. In: *The Primate Nervous System, Part I. Handbook of Chemical Neuroanatomy, Vol. 13* (Bloom FE, Bjorklund A, Hokfelt T, eds.) Elsevier, New York, 1997, pp. 39–118.
9. Whitehouse PJ, Price DL, Struble RG, Clark AW, Coyle JT, Delong MR. Alzheimer's



- disease and senile dementia: loss of neurons in the basal forebrain. *Science* 1982; **215**:1237–1239.
10. Gritti I, Mainville L, Mancina M, Jones B. GABAergic and other noncholinergic basal forebrain neurons, together with cholinergic neurons, project to the mesocortex and isocortex in the rat. *J Comp Neurol* 1997; **383**:163–177.
  11. Zaborszky L. Afferent connections of the forebrain cholinergic projection neurons, with special reference to monoaminergic and peptidergic fibers. In: *Central Cholinergic Synaptic Transmission* (Frotscher M, Misgeld U, eds.) Birkhauser, Basel, 1989, pp. 12–32.
  12. Heilman KH, Watson RT, Valenstein E. Neglect and related disorders. In: *Clinical Neuropsychology* (Heilman KM, Valenstein E, eds.) Oxford University Press, New York, 1993, pp. 279–336.
  13. Mesulam MM. Attentional networks, confusional states, and neglect syndromes. In: *Principles of Behavioral and Cognitive Neurology* (Mesulam, M.M., ed.), Oxford University Press, New York, 2000, pp.174–293.
  14. McGaughy J, Everitt BJ, Robbins TW, Sarter M. The role of cortical cholinergic afferent projections in cognition: impact of new selective immunotoxins. *Behav Brain Res* 2000; **115**:251–263.
  15. Szentagothai J. The modular architectonic principle of neural centers. *Rev Physiol Biochem Pharmacol* 1983; **98**:11–61.
  16. Gerfen CR. The neostriatal mosaic. I. Compartmental organization of projections from the striatum to the substantia nigra in the rat. *J Comp Neurol* 1985; **236**:454–476.
  17. Bjaalie JG, Diggle PJ, Nikundiwe A, Karagulle T, Brodal P. Spatial segregation between populations of ponto-cerebellar neurons: statistical analysis of multivariate interactions. *Anat Rec* 1991; **231**:510–523.
  18. Graybiel AM, Penney JB. Chemical architecture of the basal ganglia. In: *The Primate Nervous System, Part III, Handbook of Chemical Neuroanatomy, Vol. 15* (Bloom FE, Bjorklund A, Hokfelt T, eds.) Elsevier, Amsterdam, 1999, pp.227–284.
  19. Mountcastle VB. *Perceptual Neuroscience. The Cerebral Cortex*. Harvard University Press, Cambridge, MA, 1998.
  20. Malach R. Dendritic sampling across processing streams in monkey striate cortex. *J Comp Neurol* 1992; **31**:303–312.
  21. He S-Q, Dum RP, Strick PL. Topographic organization of corticospinal projections from the frontal lobe: motor areas on the lateral surface of the hemisphere. *J Neurosci* 1993; **13**:952–980.
  22. Malach R. Cortical columns as devices for maximizing neuronal diversity. *Trends Neurosci* 1994; **17**:101–104.
  23. Malmierca MS, Blackstad TW, Osen KK, Karagulle T, Molowny RL. The central nucleus of the inferior colliculus in rat: a Golgi and computer reconstruction study of neuronal and laminar structure. *J Comp Neurol* 1993; **333**:1–27.
  24. Malmierca MS, Leergard TB, Bajo VM, Bjaalie JG, Merchan MA. Anatomic evidence of a three-dimensional mosaic pattern of tonotopic organization in the ventral complex of the lateral lemniscus in cat. *J Neurosci* 1998; **18**:10603–10618.
  25. Leergard BT, Alloway KD, Mutic JJ, Bjaalie JG. Three-dimensional topography of corticopontine projections from rat barrel cortex: correlations with corticostriatal organization. *J Neurosci* 2000; **20**:8474–8484.
  26. Jacobs GA, Theunissen FE. Extraction of sensory parameters from a neural map by primary sensory interneurons. *J Neurosci* 2000; **20**:2934–2943.
  27. Sofroniew MV, Eckenstein F, Thoenen H, Cuellar AC. Topography of choline acetyltransferase-containing neurons in the forebrain of the rat. *Neurosci Lett* 1982; **33**:7–12.



28. Armstrong DM, Saper CB, Levey AI, Wainer BH, Terry RD. Distribution of cholinergic neurons in the rat brain demonstrated by immunohistochemical localization of choline acetyltransferase. *J Comp Neurol* 1983; **216**:53–68.
29. Mesulam MM, Mufson EJ, Wainer BH, Levey AI. Central cholinergic pathways in the rat: an overview based on an alternative nomenclature (Ch1–Ch6). *Neuroscience* 1983; **10**:1185–1201.
30. Rye DB, Wainer BH, Mesulam M-M, Mufson EJ, Saper CB. Cortical projections arising from the basal forebrain: a study of cholinergic and noncholinergic components combining retrograde tracing and immunohistochemical localization of choline acetyltransferase. *Neuroscience* 1984; **13**:627–643.
31. Amaral DG, Kurz J. An analysis of the origins of the cholinergic and noncholinergic septal projections to the hippocampal formation in the rat. *J Comp Neurol* 1985; **240**:37–59.
32. Carlsen J, Zaborszky L, Heimer L. Cholinergic projections from the basal forebrain to the basolateral amygdaloid complex: a combined retrograde fluorescent and immunohistochemical study. *J Comp Neurol* 1985; **234**:155–167.
33. Zaborszky L, Carlsen J, Brashear HR, Heimer L. Cholinergic and GABAergic afferents to the olfactory bulb in the rat with special emphasis on the projection neurons in the nucleus of the horizontal limb of the diagonal band. *J Comp Neurol* 1986; **243**:488–509.
34. Woolf NJ. Cholinergic system in mammalian brain and spinal cord. *Progr Neurobiol* 1991; **37**:475–524.
35. Wainer BH, Steininger TL, Roback JD, Burke-Watson MA, Mufson EJ, Kordower J. Ascending cholinergic pathways: functional organization and implications for disease models. *Progr Brain Res* 1993; **98**:9–30.
36. Mesulam MM, Geula C. Nucleus basalis (Ch4) and cortical cholinergic innervation in the human brain: observations based on the distribution of acetylcholinesterase and choline acetyltransferase. *J Comp Neurol* 1988; **275**:216–240.
37. Baskerville KA, Chang HT, Herron P. Topography of cholinergic afferents from the nucleus basalis of Meynert to representational areas of sensorimotor cortices in the rat. *J Comp Neurol* 1993; **335**:552–562.
38. Zaborszky L, Duque A. Local synaptic connections of basal forebrain neurons. *Behav Brain Res* 2000; **15**:143–158.
39. Felleman DJ, Van Essen DC. Distributed hierarchical processing in the primate cerebral cortex. *Cerebral Cortex* 1991; **1**:1–47.
40. Alloway D, Crist J, Mutic JJ, Roy SA. Corticostriatal projections from rat barrel cortex have an anisotropic organization that correlates with vibrissal whisking behavior. *J Neurosci* 1999; **19**:10908–10922.
41. Nadasdy Z, Zaborszky L. Computational analysis of spatial organization of large scale neural networks. *Anat Embryol* 2001; **204**: 303–317.
42. Valverde F. Reticular formation of the pons and medulla oblongata. A Golgi study. *J Comp Neurol* 1961; **116**:71–99.
43. Leontovich TA, Zhukova GP. The specificity of the neuronal structure and topography of the reticular formation in the brain and spinal cord of carnivora. *J Comp Neurol* 1963; **121**:347–381.
44. Ramon-Moliner E, Nauta WJH. The isodendritic core of the brain stem. *J Comp Neurol* 1966; **126**:311–336.
45. Das GD, Kreutzberg GW. Evaluation of interstitial nerve cells in the central nervous system. *Adv Anat Embryol* 1968; **41**:1–58.
46. Zaborszky L. Synaptic organization of basal forebrain cholinergic projection neurons. In: *Neurotransmitter Interactions and Cognitive Functions* (Levin E, Decker M, Butcher L, eds.) Birkhauser, Boston, 1992, pp. 27–65.

47. McMullen NT, Goldberger B, Suter CM, Glaser EM. Neonatal deafening alters nonpyramidal dendrite orientation in auditory cortex: a computer microscope study in the rabbit. *J Comp Neurol* 1988; **267**:92–106.
48. Csillik B, Rakic P, Knyihar-Csillik E. Peptidergic innervation and the nicotinic acetylcholine receptor in the primate basal nucleus. *Eur J Neurosci* 1998; **10**:573–585.
49. Braitenberg V, Schutz A. *Cortex: Statistics and Geometry of Neuronal Connectivity*. Springer, Berlin, 1998.
50. Szentagothai J. "Specificity versus (quasi-) randomness" revisited. *Acta Morph Hung* 1990; **38**:159–167.
51. Zaborszky L, Cullinan WE, Luine VN. Catecholaminergic-cholinergic interaction in the basal forebrain. *Prog Brain Res* 1993; **98**:31–49.
52. Zaborszky L, Cullinan WE, Braun A. Afferents to basal forebrain cholinergic projection neurons: an update. In: *Basal Forebrain: Anatomy to Function* (Napier TC, Kaliwas PW, Hanin I, eds.) Plenum Press, New York, 1991, pp. 43–100.
53. Zaborszky L, Gaykema RP, Swanson DJ, Cullinan WE. Cortical input to the basal forebrain. *Neuroscience* 1997; **79**:1051–1078.
54. Pang K, Tepper JM, Zaborszky L. Morphological and electrophysiological characteristics of non-cholinergic basal forebrain neurons. *J Comp Neurol* 1998; **394**:186–204.
55. Duque A, Balatoni B, Detari L, Zaborszky L. EEG correlation of the discharge properties of identified neurons in the basal forebrain. *J Neurophysiol* 2000; **84**:1627–1635.
56. Schwaber JS, Rogers WT, Satoh K, Fibiger HC. Distribution and organization of cholinergic neurons in the rat forebrain demonstrated by computer-aided data acquisition and three-dimensional reconstruction. *J Comp Neurol* 1987; **263**:309–325.
57. Cullinan WE, Zaborszky L. Organization of ascending hypothalamic projections to the rostral forebrain with special reference to the innervation of cholinergic projection neurons. *J Comp Neurol* 1991; **306**:631–667.
58. Gaykema RPA, Zaborszky L. Direct catecholaminergic-cholinergic interactions in the basal forebrain: II. Substantia nigra and ventral tegmental area projections to cholinergic neurons. *J Comp Neurol* 1996; **374**:555–577.
59. Glaser JR, Glaser EM. Neuron imaging with Neurolucida—a PC-based system for image combining microscopy. *Comput Med Imaging Graph* 1990; **14**:307–317.
60. Vassbo K, Nicotra G, Wiberg M, Bjaalie JG. Monkey somatosensory cerebrotocerebellar pathways: Uneven densities of corticopontine neurons in different body representations of areas 3b, 1, and 2. *J Comp Neurol* 1999; **406**:109–128.
61. Heimer L, Zaborszky L. (eds.) *Neuroanatomical Tract-Tracing Methods 2. Recent Progress*. Plenum Press, New York, 1989.